PNAS RESEARCH ARTICLE | APPLIED PHYSICAL SCIENCES

Actuating superparamagnetic nanoparticle monolayers

Edward P. Esposito[a,b,1], Hector Manuel Lopez Rios[c,1], Monica Olvera de la Cruz[c,d,e,f,2], and Heinrich M. Jaeger[a,b,2]

Affiliations are included on p. 8.

Contributed by Monica Olvera de la Cruz; received November 19, 2024; accepted February 24, 2025; reviewed by Sibani L. Biswal and David W. Marr

Magnetically responsive, mechanically flexible microstructures are desirable for applications ranging from smart sensors to remote-controlled actuation for surgery or robotics. Embedding magnetic nanoparticles into a thin matrix of elastic material enables high flexibility while exploiting the magnetic response of the individual particles. However, in the ultrathin limit of such nanocomposite materials, the particles become too small to sustain a permanent dipole moment. This implies that now large magnetic field gradients are required for actuation, which are difficult to achieve with externally applied fields. Here, we demonstrate through experiment and simulation that monolayer sheets of close-packed paramagnetic nanoparticles in a uniform applied field can generate large local field gradients through particle interactions. As a result, a strong collective magnetization is obtained that leads to large deflections of freestanding sheets already in moderate applied fields. Exploiting the vector nature of the applied field, we furthermore find that it is possible to induce more complex curvature and twist the sheets. Finally, we show that paramagnetic nanoparticle monolayers applied as coatings can generate sufficient force to deflect strips of nonmagnetic material that is several orders of magnitude thicker.

magnetoelastic | superparamagnetic | nanoparticles

Significance

Nanometer-thin elastic sheets containing embedded magnetic particles offer special opportunity for remote actuation by magnetic fields because their small thickness endows them with extreme mechanical flexibility. However, in this ultrathin limit, the embedded particles lose their normal magnetic property and become paramagnetic, which typically limits the magnetic responsiveness of the structure. We show that this limitation can be overcome with self-assembled monolayers of magnetic nanoparticles, where the particles pack densely and interact sufficiently strongly that even uniform applied fields produce an actuation response well beyond the linear regime. Such ultrathin magnetic sheets can generate large forces and could find applications also as coatings to actuate nonmagnetic structures

Since magnetic materials tend to be brittle and stiff, recent work on magnetic actuation has focused on the bending of composites made of deformable nonmagnetic materials with embedded magnetic particles (1–6). The particles experience forces due to interactions with an applied field, and the forces induce the bending when the structure is sufficiently soft or flexible. For the largest bending, it is desirable to use ultrathin materials to maximize their flexibility while at the same time using high particle density to generate the largest forces. This has found recent applications in micro- or nano-actuation (7–9), with extensions to flexible electronics (10) and especially microrobotic locomotion (11, 12).

When the particles have permanent dipole moments, the behavior of such structures can be well-understood as the thin limit of hard-magnetic soft materials (7–9, 13, 14). The mechanics are then straightforward because the permanent dipoles are independent of the applied magnetic field, so that material deformations involve direct relationships between the external field, the dipole positions, and the forces experienced by the material (14, 15). However, once the nanoparticles are too small to retain a permanent dipole moment, they instead behave as paramagnets (16). The behavior of such composite materials can now be best understood as the thin limit of soft-magnetic soft materials (7). The mechanics are considerably more complex in this case because dipole moments are no longer independent of the external field or of each other (17, 18). Despite these complexities, thin superparamagnetic composites may offer practical advantages over ferromagnetic composites in some applications since their hysteresis-free magnetization limits magnetic interactions in the absence of an externally applied field.

Correctly predicting the bending deformation of thin soft-magnetic soft materials requires accurate modeling of the magnetic forces, in turn requiring an accurate description of how the particle dipole moments align in the applied field. Prior work on large bending of soft magnetoelastic beams commonly assumes a completely in-material alignment of magnetic moments together with a linear magnetization response to the applied field (19–21). These assumptions, corresponding to magnetization dominated by dipole–dipole interactions in the small field regime, work well for sufficiently soft or flexible bulk magnetoelastic materials. However, the magnetic forces generated in the small field regime may be too small to bend many nano-scale systems which tend to have tensile stiffnesses on the order of 1 to 10 GPa (22–24). It is also not clear whether in-material magnetization is a good assumption for quasi-2D systems. Indeed, some recent work on ultrathin magnetoelastic systems assumes a magnetization that always follows

Author contributions: M.O.d.l.C. and H.M.J. designed research; E.P.E. and H.M.L.R. performed research; E.P.E., H.M.L.R., M.O.d.l.C., and H.M.J. analyzed data; and E.P.E., H.M.L.R., M.O.d.l.C., and H.M.J. wrote the paper.

Reviewers: S.L.B., Rice University; and D.W.M., Colorado School of Mines.

The authors declare no competing interest.

[1]E.P.E. and H.M.L.R. contributed equally to this work.

[2]To whom correspondence may be addressed. Email: m-olvera@northwestern.edu or jaeger@uchicago.edu.

This article contains supporting information online at https://www.pnas.org/lookup/suppl/doi:10.1073/pnas.2424073122/-/DCSupplemental.

Published March 26, 2025.

the applied field (25–27), corresponding to an independent (or fixed) dipole model as commonly used in studies of colloidal magnetism (28–30).

In this work, we relax such assumptions about the field or the magnetization. We study paramagnetic nanoparticle (NP) monolayer sheets through experiments and simulations to understand their mechanics in the nonlinear magnetization regime of large magnetic fields and forces. Experimental sheets consist of Fe_3O_4 NPs of diameter 12.25 nm self-assembled into the 20 μm × 20 μm square NP sheets pictured by transmission electron (TEM) and optical microscopy (Fig. 1 *A* and *B*). Each NP's surface is coated with a single layer of short oleic acid molecules. These ligand molecules act as spacers and provide the elastic matrix that holds the sheets together by van der Waals interactions between ligands on neighboring particles (1.75 nm around each particle; visible in the TEM image as the light gray region between the darker gray nanoparticle cores) (24, 31). NP sheets that have torn partially free from the copper support, as highlighted in white in Fig. 1*B*, are subjected to uniform external magnetic fields $\mathbf{B}_{\text{ext}}$ generated by an array of permanent magnets as depicted in Fig. 1*C*. The sheets' surface height $z(x, y)$, and especially the free corner deflection δ, is measured by confocal microscopy as the field is varied. Fig. 1*D* shows the initial and final state of a NP sheet simulated by Molecular Dynamics (MD). Each NP is modeled directly in the simulation, having its own dipole moment vector $\mathbf{m}_i$, oriented at an angle $\theta_{m,i}$ from the vertical. Simulated NPs are separated from their immediate neighbors by a center-to-center rest distance of $r_0 = 15.75$ nm just as their counterparts in the experiments. We allow the dipole moments to evolve freely according to both the external magnetic field and the field generated by all other dipoles (28).

Using moderate-to-large fields in which NP magnetic moments approach saturation, we observe the NP sheets bending far into the nonlinear regime. Although we apply uniform magnetic fields, the system nevertheless experiences large forces due to the high density of dipoles. We find that neither the dipole–dipole nor the Zeeman interactions dominate the induced magnetization, and the trade-off between them, especially with saturating particles, leads to nontrivial magnetization states not conforming to either limit. We show how the induced dipole moments depend on the local configuration of the sheet and use them to calculate the magnetic forces. By comparing deflections from experiments and simulations, we find a master curve that predicts the deflection of such a system for various magnetic and elastic parameters. We then extend these findings by demonstrating how dipole forces can generate not only bending deflections but also twist and, when applied in ultrathin coatings, how they can produce forces sufficiently strong to actuate much thicker nonmagnetic sheets.

Theoretical Background

A magnetoelastic sheet composed of discrete magnetic particles embedded in an elastic medium can be characterized by its configuration, the set of all particle locations $\{\mathbf{r}_i\}$, and its magnetization state, the set of all particle magnetizations $\{\mathbf{m}_i\}$. When subjected to an applied field $\mathbf{B}_{\text{ext}}$, the system responds by finding a configuration and magnetization state minimizing a total energy functional that may be separated into static elastic and magnetic functionals as $U(\{\mathbf{r}_i\}, \{\mathbf{m}_i\}, \mathbf{B}_{\text{ext}}) = U_{\text{el}}(\{\mathbf{r}_i\}) + U_{\text{mag}}(\{\mathbf{r}_i\}, \{\mathbf{m}_i\}, \mathbf{B}_{\text{ext}})$. For a thin plate, the elastic energy generally separates further into functionals representing decoupled stretching and bending, $U_{\text{el}}(\{\mathbf{r}_i\}) = U_s(\{\mathbf{r}_i\}) + U_b(\{\mathbf{r}_i\})$ (32).

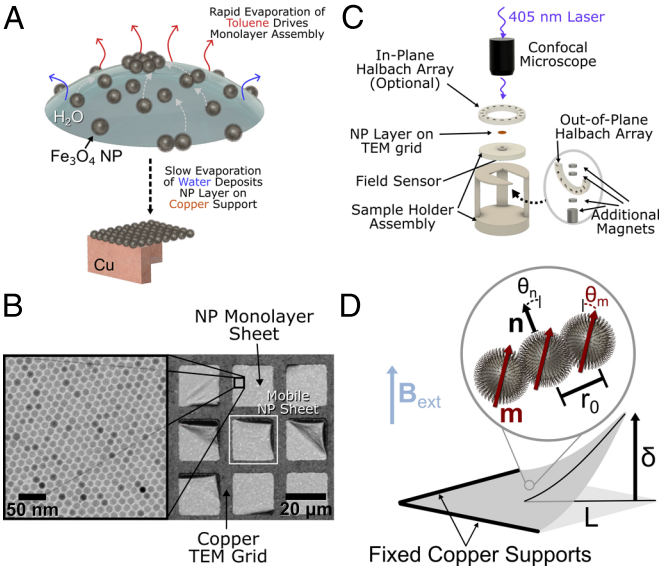

Fig. 1. NP Sheet formation and measurement. (*A*) Self-assembly and deposition of nanoparticle sheets (schematic). (*B*) Characteristic TEM (*Left*) and optical (*Right*) micrographs of NP monolayer sheet on a copper TEM grid. Sheets that have torn partially free from the copper, as the one highlighted in the *Right* image, can deflect and are measured in subsequent experiments. (*C*) Experimental setup in vertically exploded view. NP sheets on TEM grid are subjected to magnetic fields generated by permanent magnets in cylindrical Halbach arrays, with additional magnets added to control the field strength, as measured with a linear Hall sensor. The deflected sheet's surface is imaged by confocal reflectance microscopy. (*D*) NP sheet geometry and parameters.

For a static micromagnetic system, the magnetic energy will generally separate into terms representing the coupling of particle magnetization with the external field and with the field generated by the other dipoles, $U_{\text{mag}}(\{\mathbf{r}_i\}, \{\mathbf{m}_i\}, \mathbf{B}_{\text{ext}}) = U_{\text{zee}}(\{\mathbf{m}_i\}, \mathbf{B}_{\text{ext}}) + U_{\text{dip}}(\{\mathbf{r}_i\}, \{\mathbf{m}_i\})$. Since Fe_3O_4 has weak magnetocrystalline anisotropy (33), and since shape effects are minimal for our quasi-spherical particles, we disregard anisotropy energy. And we disregard exchange coupling between nanoparticles due to the ∼2.7 nm core–core separation, since iron atoms on neighboring NPs are at least that far apart.

For a system of discrete paramagnets, the magnetizations are coupled to the configuration through some function $\mathbf{m}_i(\{\mathbf{r}_i\}, \mathbf{B}_{\text{ext}})$. We model the nanoparticles as point paramagnets using a mutual dipole model (MDM), standard in studies of magnetic colloids (12, 28, 34–36) but uncommon in magnetoelasticity. In particular, we use a magnetization function

$$\mathbf{m}_i(\mathbf{B}_i) = m_{\text{sat}}\mathcal{L}(|\mathbf{B}_i|/B_{\text{sat}})\frac{\mathbf{B}_i}{|\mathbf{B}_i|}, \qquad [1]$$

where $\mathcal{L}(x) = \coth(x) - 1/x$ is the Langevin function, $\mathbf{B}_i = \mathbf{B}(\mathbf{r}_i)$ is the total magnetic field experienced by particle i, m_{sat} is the saturation magnetization of the nanoparticles, and B_{sat} is a parameter measuring how strong a field will nearly saturate the particles (related to their initial susceptibility as $\chi_0 = m_{\text{sat}}/B_{\text{sat}}$). Additionally, the total magnetic field $\mathbf{B}_i = \mathbf{B}_{\text{ext}} + \mathbf{B}_{i,\text{dip}}$ at particle i, includes both the external field and the field due to all of the other dipoles

$$\mathbf{B}_{i,\text{dip}} = \sum_{j\neq i}\frac{\mu_0}{4\pi r_{ij}^3}\left[3(\mathbf{m}_j\cdot\hat{\mathbf{r}}_{ij})\hat{\mathbf{r}}_{ij} - \mathbf{m}_j\right] \qquad [2]$$

in which $\mathbf{r}_{ij} = \mathbf{r}_i - \mathbf{r}_j$, $r_{ij} = |\mathbf{r}_{ij}|$, and $\hat{\mathbf{r}}_{ij} = \mathbf{r}_{ij}/r_{ij}$. Once the magnetization has been calculated for a given configuration, the

dipole forces can be evaluated through the relation $\mathbf{F}_i = (\mathbf{m}_i \cdot \nabla)\mathbf{B}_{i,dip}$ and then used to generate a new configuration (the magnetic force expression written exclusively in terms of the magnetization, after applying the gradient to Eq. **2**, is given in *SI Appendix*). New mechanical configurations and new sets of magnetic forces are calculated in alternation until the whole system reaches a steady mechanical configuration.

Results and Discussion

Deflections in Uniform Fields. Fig. 2*A* shows the 3D confocal data for one experimental sheet with and without magnetic field. Scans are typically taken over a range of external magnetic field strengths from $B_{ext} = 0$ to 0.15 T, and Fig. 2*B* shows the surface height along the line trace of the diagonal depicted in the *Upper Left* corner for each strength. The deflection of the free corner traces a characteristic S-shaped curve as shown in the *Lower Inset*, initially curved for weak external fields, and seeming to saturate for large fields. Fig. 2*C* shows the results from many such experiments and simulations, collapsed by a fitting function

$$\delta(B_{ext}) = \delta^* \frac{{B_{ext}}^{\alpha}}{{B^*}^{\alpha} + {B_{ext}}^{\alpha}}, \qquad [3]$$

a generic class of sigmoid function that is 0 for $B_{ext} = 0$ and saturates to a value δ^*, attaining half saturation at $B_{ext} = B^*$ (generally different from B_{sat}). The curvature is controlled by the power α, found to be 1.8 from sheets simulated with different stiffnesses (see *SI Appendix* for why this particular fitting function was chosen). The *Inset* of Fig. 2*C* shows the uncollapsed data, together with the fitting functions using $\alpha = 1.8$ as found in the simulations. The uncollapsed deflections are normalized by the linear scale L due to the difference in size between the experimental and simulated sheets.

Given the particle magnetization function Eq. **1**, we can understand why some function like our Eq. **3** must fit well to the data. In our sheets with strong forces between densely packed dipoles, we can think of the dipole–dipole forces per unit area as a type of pressure loading. For thin plates generically, at small pressures p the deflection will scale as $\delta \sim p$, while for larger pressures, the deflection will instead scale as $\delta \sim p^{1/3}$ (32). The pressure here results from all of the induced magnetizations and is not related to the external field strength in a simple form. Well below saturation however, the induced dipole moments scale roughly linearly with the applied field, and since the forces scale as the product of the induced magnetic moments and the dipole field, itself scaling proportionally with the dipole moments, the pressures scale roughly quadratically with the dipole moments. If the induced dipole moments were strictly linear in the small field regime, we would then expect a quadratic scaling of the deflection with the external field strength and a power of $\alpha = 2$ in Eq. **3**. The value found, $\alpha = 1.8$, is consistent with the sublinearity of the magnetization function Eq. **1**. Once the particles begin to saturate and the induced magnetization stops increasing with the applied field (only reorienting closer to the external field; see Fig. 3 and the subsequent discussion), the forces will also stop increasing with the applied field. As the magnetic forces change less and less, the deflection saturates. The saturated value δ^* from Eq. **3** should then be a deflection corresponding to the largest balance between the magnetic energy (the maximal loading) and the elastic energy (the maximal deformation). From MD simulations of sheets with different Young's moduli, we find that

$$\frac{\delta^*}{L} \approx \exp \frac{\frac{-Et^3}{12(1-\nu^2)}}{Nm_{sat}B_{sat}}, \qquad [4]$$

where the argument of the exponential is the ratio between the scales of magnetic energy and bending energy. E is the sheet's Young's modulus, t is the thickness (taken as the diameter of the magnetic particles), ν is the Poisson's ratio, and N is the number of particles in the sheet. If the magnetic scale far exceeds the bending scale, magnetic forces can be large enough to overcome the bending rigidity and produce deflections approaching the linear scale of the sheet. For the softest of our sheets, the largest measured deflections of $\delta/L \approx 0.75$ correspond to the free corner of the sheet bending through an angle of roughly 50°. In such cases, δ^*/t exceeds 1,000, far into the nonlinear plate bending regime. To test whether these fit values of δ^* correspond sensibly to the typical stiffnesses of the sheets, we used the saturation deflection values found from fitting our experimental curves together with other known or presumed material parameters to calculate a "measured" Young's modulus. The distribution of moduli obtained in this way corresponds well to the distribution of moduli from direct measurements of similar sheets using AFM indentation tests, following the technique of Wang et al. (37). Variability in the flexibility of experimental sheets can be explained in part

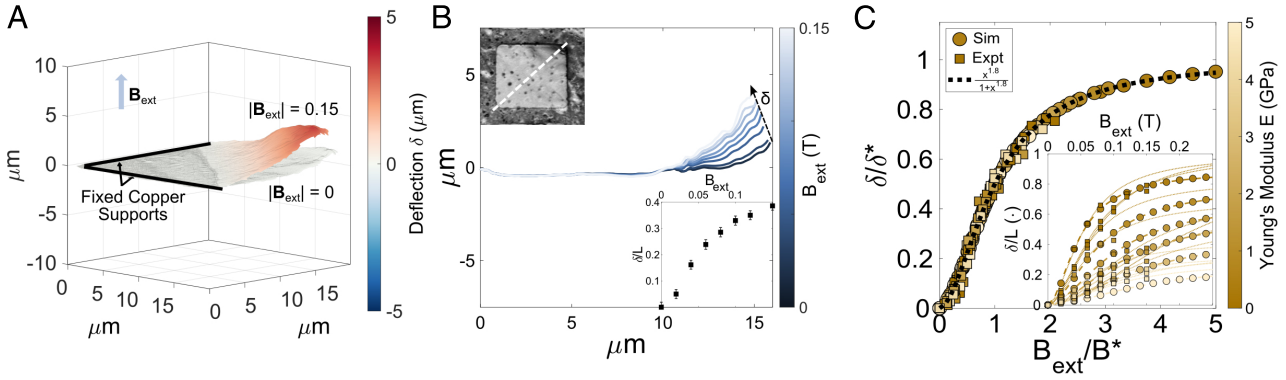

Fig. 2. Nanoparticle sheet deflection in applied external B-field. (*A*) Confocal microscopy scans of a sheet without and with applied field. (*B*) Sheet deflection profiles for increasing *B*. *Upper Left Inset*: Optical micrograph of the sheet. The dashed line indicates line scans for the deflection profiles. *Lower Right Inset*: Vertical deflection δ of the free corner of the sheet, normalized by the length L of the actuatable portion of the profile (in this case approximately half the diagonal of the square sheet). (*C*) Experimental and simulated deflections collapsed by the fitting function given by Eq. **3**. *Inset*: Normalized deflection as a function of applied field from experiments on different sheets (squares) and simulations for Young's moduli from 0.5 to 5 GPa (circles).

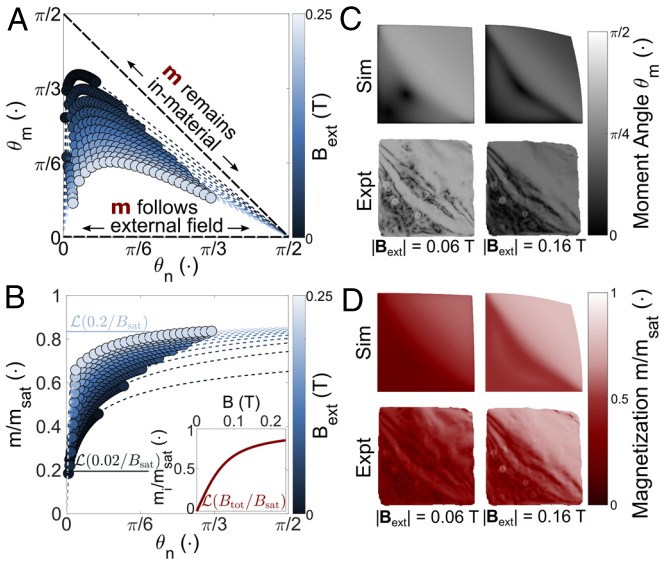

Fig. 3. Magnetization direction and magnitude in nanoparticle sheets. (*A*) Average single particle magnetization direction θ_m as function of local surface orientation θ_n from molecular dynamics (MD) simulations. Distributions of θ_m for given θ_n were extracted from simulated sheets actuated by different external field magnitudes. The angles θ_m and θ_n represent the deviations of the particle magnetic moments and of the local sheet normal from the direction of the applied field, respectively. If $\theta_m = \pi/2 - \theta_n$, then the magnetization remains in-plane. Dots: Averages from simulation. Dashed lines: Fitting function described in the text. (*B*) Average magnetization as a function of local surface orientation for a range of external field strengths. Note how flat orientations of the sheet tend to suppress the magnetization due to stronger demagnetizing fields. *Inset*: Single particle Langevin magnetization function. (*C*) Low-field and high-field moment angle, evaluated directly for the simulation and indirectly for the experiments. Using surface normals extracted from the confocal microscopy scans, we calculated experimental magnetic moments using the fitting functions described in the text, Eq. **5**. (*D*) Same as (*C*), but for the moment magnitude.

by imperfections in the spatial arrangements of the NPs (see *SI Appendix* for details of the effects of local holes in particular).

Nonuniform Magnetization States. An isolated paramagnetic particle responds to an external field through Eq. **1** with only the applied field, as $\mathbf{m} = m_{\text{sat}}\mathcal{L}(|\mathbf{B}_{\text{ext}}|/B_{\text{sat}})\mathbf{B}_{\text{ext}}/|\mathbf{B}_{\text{ext}}|$, since there is no field from other dipoles. In particular, its magnetic moment aligns fully with the applied field direction so that the angle between the moment and the field θ_{m} is zero, while the strength of the moment is $m = m_{\text{sat}}\mathcal{L}(|\mathbf{B}_{\text{ext}}|/B_{\text{sat}})$. When many such particles are packed closely together, the dipole field in Eq. **2** becomes appreciable relative to the applied field, so the total field experienced by the particles may be stronger or weaker than the applied field, and will generally not be in the same direction as the applied field. Since the dipole moment follows the total field direction, θ_{m} may no longer be zero, while m may also differ from $m_{\text{sat}}\mathcal{L}(|\mathbf{B}_{\text{ext}}|/B_{\text{sat}})$. The dipole field experienced by any particle depends strongly on the position and magnetization of neighboring particles, and the locations of neighboring particles contributing most to that dipole field can be characterized simply by the local surface normal. We therefore expect particle dipole moments to vary strongly with the angle θ_{n} between the local surface normal and the applied field. Fig. 3*A* demonstrates this variation with the local normal of simulated sheets of 1 GPa stiffness actuated at various external field strengths (averaged over all particles in the simulated sheet with the various normal directions at the equilibrated sheet configuration), while Fig. 3*B* shows how the magnitude of the magnetization varies. We find that the strength and direction of the particle moments from simulated actuated sheets are well described as functions of the local surface normal direction θ_n, irrespective of the sheet's stiffness (*SI Appendix*, Fig. S6), by

$$m(\theta_{\text{n}}) = m^* \frac{\theta_{\text{n}}^{1/2}}{\theta_{\text{n}}^{*1/2} + \theta_{\text{n}}^{1/2}}$$
$$\theta_{\text{m}}(\theta_{\text{n}}) = c_0 \frac{\theta_{\text{n}}(\frac{\pi}{2} - \theta_{\text{n}})}{\theta_{\text{n}} - \theta_{\text{n}}^{**}}. \qquad [5]$$

Here, m^*, θ_n^*, c_0 and θ_n^{**} are fit parameters that depend on the external field, as well as material properties like m_{sat}, B_{sat} and r_0. As the sheet rotates into the applied field (i.e. as the sheet's normal rotates away from the applied field), the competition between the Zeeman and dipole energy terms reduces, and so the magnetization directions simultaneously approach both the tangent plane of the sheet and the applied field. As the external field strength is increased, the magnetization approaches the field direction more closely at all orientations of the local normal. This latter behavior is due to the fact that the particles saturate, limiting the magnitude of the dipole–dipole energy, whereas the Zeeman energy continues increasing linearly with the applied field. For saturated particles, increasing the field strength increases the ratio of Zeeman to dipole–dipole energy, favoring closer alignment of the particle magnetization directions with the applied field. This competition between Zeeman and dipole–dipole energies is especially visible through the maxima of the θ_{m} curves because the maximum deviation occurs at the surface orientation where the two energies nearly balance. The maximum deviation decreases for increasing fields because the Zeeman energy increases linearly while the dipole–dipole energy saturates at high fields. We also note that the maximal deviation from the applied field occurs at larger deviations of the surface angles, which also results from the saturation of the dipoles since after saturation, the sheet must rotate further in order for the dipole–dipole energy to compete with the increasing Zeeman energy.

In Fig. 3 *C* and *D*, we compare the magnetic response of experimental and simulated sheets using Eq. **5** to calculate experimental magnetic moments with surface normals extracted from the confocal microscopy height maps $z(x, y)$. Because of the variation of surface normals across the sheet, Fig. 3 *C* and *D* display a distribution of magnetic moment strengths and orientations. In the free portion where deflections are large, the normal makes its largest angle with the applied field, and the strength of the magnetization is largest. In such regions, the dipole–dipole and Zeeman interactions favor dipole orientations in similar directions, resulting in local dipole fields that enhance the external field, $|\mathbf{B}| > |\mathbf{B}_{\text{ext}}|$, leading in turn to a collectively greater magnetic moment than in an array of independent dipoles. By contrast, in the fixed portion of the sheet, which remains relatively flat, dipole–dipole and Zeeman interactions favor magnetization orientations in competing directions, resulting in local dipole fields that oppose the external field, $|\mathbf{B}| < |\mathbf{B}_{\text{ext}}|$, and therefore a reduced magnetic moment compared with independent dipoles. Enhancement or reduction of the magnetization relative to independent dipoles can be seen in Fig. 3*B*, where two horizontal lines have been added to show the independent dipole magnetization for low and high fields, 0.02 and 0.2 T, respectively. In all cases, we can understand variation of the magnetic moments in terms of the changing surface orientation as shown in Fig. 3 *A* and *B*.

That dipole moment directions generally differ from both the applied field direction and the local tangent plane is a complexity not usually included in prior magnetoelastic studies. Some past works studying flexible paramagnetic rods assume magnetization

always in the applied field direction (21, 38, 39). Scherbakov and Winklhofer consider a beam with distributed paramagnetic material in which the magnetization is confined to the beam axis. Gerbal et al. consider beams embedded with superparamagnetic particles (20) and compare a model in which the beams magnetize in the applied field direction against a model in which they always magnetize along their axis. Their work demonstrated that only axial magnetization would reproduce their experimental results. The implicit assumption behind such models is that axial magnetization arises through the interdependent magnetization of the distributed superparamagnetic material. Although this could arise from the interactions of a high density of superparamagnetic material, we point out that the superparamagnetic material in ref. 20 consists of rods which themselves have a strong axial anisotropy and could be explained also on that basis. In our quasi-2D MDM system in which the superparamagnetic particles do not have a strong shape or magnetocrystalline anisotropy (33), despite the high density of particles, we find that the particle magnetization always lies somewhere between the applied field and the local tangent plane. The direction of the forces acting on the particles is therefore different from what either axial or in-field magnetization models would predict, so the deflections of our system are not well-described by those models.

Magnetic Forces without External B-Field Gradients. After calculating the particle magnetic moments, we may evaluate the magnetic forces between them. We expect dipole–dipole forces even in a uniform external field because the total field can have a gradient (except for the special case of an infinite flat sheet, see *SI Appendix*). As discussed above, the magnitude of the dipole–dipole forces depends roughly quadratically on the magnitude of the magnetizations, having a scale of $\frac{\mu_0 m_{sat}^2}{4\pi r_0^4} \approx 2.7 \times 10^{-13}$ N. Experimental fields controlled by permanent magnets use Halbach cylinder arrays in order to reduce external gradients. The largest gradients in the experiments were roughly 200 T/m, which can produce forces only up to 1.45×10^{-16} N for fully saturated particles, orders of magnitude smaller than the forces between the dipoles themselves. We therefore neglect forces due to the gradients in the external field and assume that the only forces present are due to dipole–dipole interactions.

The direction of the forces depends on the directions of the particle dipole moments. We therefore expect variation in both the magnitude and directions of the dipole forces according to the variations in the dipole moments across the sheet. Fig. 4*A* demonstrates this variability with an example of a sheet deflected at moderate field strength. Arrows representing the force per particle are superposed on the configuration of the sheet, with black arrows representing the full force while green and brown arrows represent the normal and tangential force components. It is most striking that the magnitude of forces on the edge particles is much larger than on particles within the bulk area, and also that the total force is significantly different from the normal force, since both the green and black arrows are visible. We show a zoomed view of one region of the bulk to emphasize that the tangential forces are a significant component of the total force, indeed even exceeding the normal force for the region chosen.

To test the importance of the normal and tangential force components, we performed purely elastic simulations using only one force component from the magnetoelastic simulation at each field strength and compared the deflections from these partial simulations with those from the full simulation. The results are presented in Fig. 4*B*. Despite the normal and tangential forces' being of similar magnitude, the normal forces alone very nearly

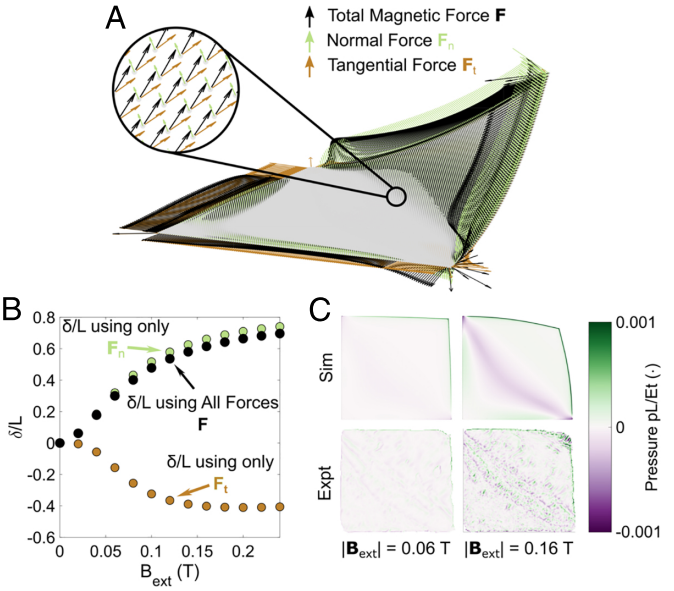

Fig. 4. Nonuniform magnetic pressures. (*A*) Simulated sheet at large applied field, with force per particle depicted by arrows. Black arrows: Total force. Green and brown arrows: Normal and tangential force components, respectively. The forces vary across the sheet, the strongest are near and at the edges. The normal and tangential components are typically of similar magnitude, as seen from the zoomed-in view, where the tangential component even exceeds the normal component. (*B*) Deflection of an initially flat sheet using only the normal or only the tangential force components. Black circles: Data from full magnetoelastic simulation as in Fig. 2. Green and brown circles: Purely elastic simulation applying only the normal (green) or tangential (brown) force components found in the magnetoelastic simulation. (*C*) Normal force distribution at low and high fields for simulated and experimental sheets. These images show the nonuniform nature of the magnetic forces, with normal pressures even changing sign across the sheet. Normal pressures for experimental sheets are calculated using the pairwise dipole–dipole force equations between the pixels representing the sheet after obtaining their magnetic moments as in Fig. 3 *C* and *D*.

reproduce the full magnetoelastic deflections, consistent with the analysis of magnetoelastic work and energy given by Brown (40). Perhaps more surprisingly, the tangential forces alone produce sizable deflections of opposite sign, likely an indication of the buckling instability of the flat sheet under compressive forces. Note how the true deflection is not simply the sum of the two partial deflections in this nonlinear deflection regime. Because they are the essential forces behind the measured sheet deflection, Fig. 4*C* shows the distribution of normal forces across the sheet, recast as a dimensionless normal pressure $\tilde{p} \equiv \frac{pL}{Et}$. The simulated pressures are the force on each particle divided by its cross-sectional area. Experimental pressures use the magnetic moments extracted from surface normals as in Fig. 3 *C* and *D* to calculate the total force on each pixel from pairwise dipole–dipole forces between pixels projected in the local normal direction. The scaling for the normal pressure used here accounts for the different sizes of the experimental and simulated sheets. Since the deflection scales cubically with the pressure load as $\delta^3 \sim \frac{pL^4}{Et}$ according to the Föppl-von Kármán plate equations (32), the dimensionless deflection $\tilde{\delta} \equiv \frac{\delta}{L}$ therefore scales with the pressure as $\tilde{\delta}^3 \sim \frac{pL}{Et}$. The magnetic force distributions are visually striking because of their nonuniformity. The normal forces not only vary in magnitude but even change sign across the sheet.

Deflections Under Different Field Orientations. One initially surprising observation in our experiments was that vertical magnetic fields cause the sheet to bend in the same direction

regardless of the polarity of the field. This suggests that the nanoparticles do not retain their magnetic moments in the absence of the external field, or at the very least that all experimental fields were larger than the coercive field for the particles. Under the transformation $\mathbf{m}_j \rightarrow -\mathbf{m}_j$ in which all dipoles change their sign, the dipole field will also change its sign. The force on each dipole will then remain unchanged: $\mathbf{F}_i \rightarrow (-\mathbf{m}_i \cdot \nabla)(-\mathbf{B}_{i,dip}) = (\mathbf{m}_i \cdot \nabla)\mathbf{B}_{i,dip}$. We therefore expect that only the strength and the axis of the external field impact the deflection of the sheet.

To determine the effect of changing the direction of the applied field, we now fix the strength but allow the field to adopt any orientation in space in our simulations, with results as depicted in Fig. 5 for a 1 GPa sheet. The field is then described by $\mathbf{B}_{ext} = B_{ext}(\sin\theta\ \cos\phi\ \hat{\mathbf{x}} + \sin\theta\ \sin\phi\ \hat{\mathbf{y}} + \cos\theta\ \hat{\mathbf{z}})$. If we fix the field at some nonzero polar angle θ and allow the field to rotate around the vertical axis so that ϕ varies from 0 to 2π, we see that the free corner of the plate achieves its maximum deflection when the field points along the $\frac{\hat{\mathbf{x}}+\hat{\mathbf{y}}}{\sqrt{2}}$ axis ($\phi = \pi/4$), and that the deflection of the free corner tends to zero as the field approaches the $\frac{-\hat{\mathbf{x}}+\hat{\mathbf{y}}}{\sqrt{2}}$ axis ($\phi = 3\pi/4$). We define $\Delta\phi = \phi - \pi/4$, which characterizes the azimuthal angle between the applied field and the free diagonal of the sheet. The effect of the rotating field is displayed in Fig. 5*B* as $\Delta\phi$ varies from 0 to $\pi/2$. If instead we fix the azimuthal angle ϕ and vary the field's polar angle from $\theta = 0$ to $\theta = \pi$, the field rotates away from the vertical, passing through the diagonal of the sheet from the fixed corner to the free corner. The deflection of the free corner of the sheet follows the applied field as shown in Fig. 5*C*, achieving its maximum magnitude for fields fully normal to the flat sheet, and passing through zero when the field is in the plane of the flat sheet. For field orientations in the plane of the flat sheet (i.e. $\theta = \pi/2$), the deformations are wholly confined to the plane and the sheet remains flat for all azimuthal orientations $\Delta\phi$. However, in case the field retains some component in the vertical direction, when the field is rotated around the vertical axis (increasing $\Delta\phi$), the sheet deforms out of the neutral plane by twisting about the $\frac{\hat{\mathbf{x}}+\hat{\mathbf{y}}}{\sqrt{2}}$ axis as much as possible in order simultaneously align the dipoles with each other and with the field. This twisting effect is depicted for a shallow field orientation of $\theta = 5\pi/12$ in Fig. 5*D*, where the line traces represent the out-of-plane deflection along the diagonal pictured in the *Inset*. The *Inset* displays the out-of-plane deflection in the case with the largest twisting, for which $\Delta\phi = \pi/2$. In this case, the free corner of the sheet remains at zero, and the maximum out-of-plane deflection of the sheet is attained along the free edges.

Since we find that the deflection of the free corner does not fully characterize the out-of-plane deformation of the plate, we therefore cast the sheet's configuration as a superposition of two deformation modes, a bending (i) and a twisting (ii) mode as demonstrated in Fig. 5*A*. The two modes are well described by cubic and sinusoidal functions respectively, as can be seen from the diagonal line traces in Fig. 5*C* for mode (i) and from the lightest diagonal trace in Fig. 5*D* for mode (ii). The full shape is well described by their superposition $a_i(\mathrm{i}) + a_{ii}(\mathrm{ii})$, where $a_{ii} = 1 - a_i$ and $0 \leq a_i \leq 1$. Modes (i) and (ii) are determined as functions of θ by fitting mode (i) for $\Delta\phi = 0$ and mode (ii) for $\Delta\phi = \pi/2$. The mode weights a_i and a_{ii} are then determined

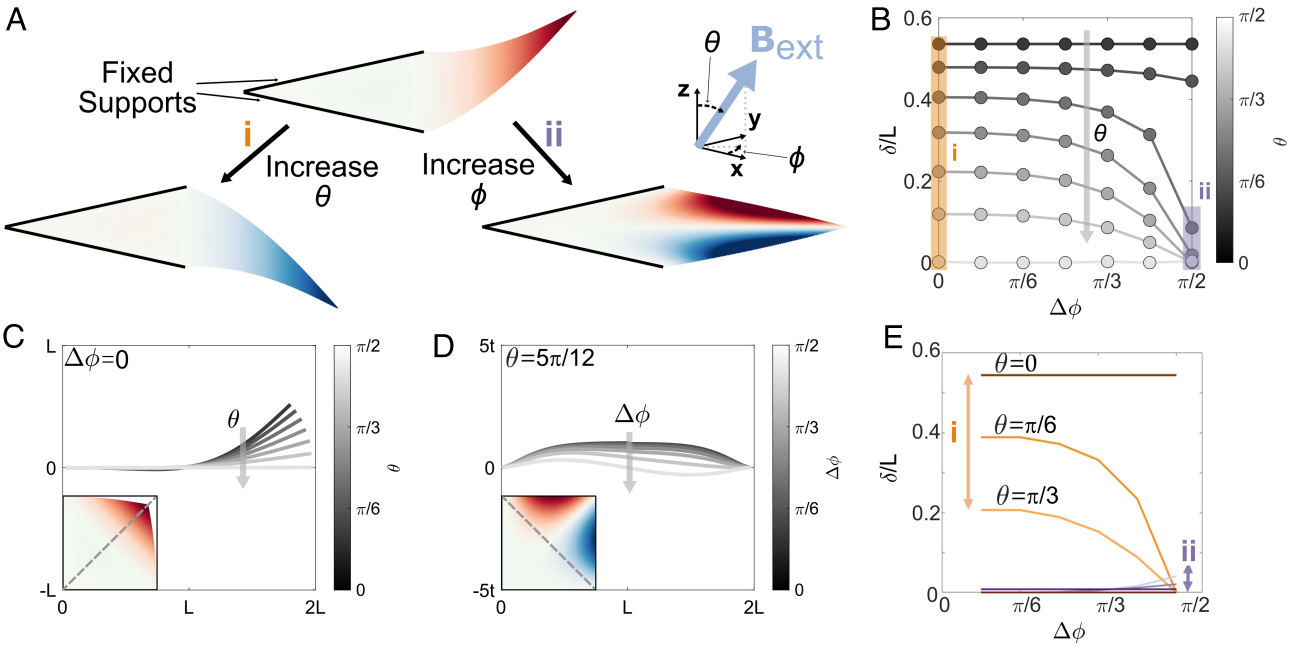

Fig. 5. Twisting sheets by changing the applied field orientation. (*A*) Deflections in fields with general direction are characterized by two modes: Mode i corresponds to deflection along the free diagonal; mode ii corresponds to twisting around the mode i diagonal, leading to undulations in the perpendicular direction. Red, blue: positive and negative deflections respectively. (*B*) End deflection of 1 GPa sheet at constant field strength (here, $B_{ext} = 0.12$ T) but varying direction. At fixed ϕ and increasing θ, the field rotates away from the vertical and deflection decreases. At fixed θ but increasing ϕ, the field rotates around the vertical axis, and for fields with substantial components in the xy plane, end deflection vanishes abruptly as the field rotates away from the free corner. (*C*) Deflection profiles for different θ at $\Delta\phi = 0$, corresponding to mode i. *Inset*: 2D projection of simulated sheet with $\theta = \frac{\pi}{12}$ and $\Delta\phi = 0$, as an example of large mode (i) deflection; profiles evaluated along dashed line. (*D*) Deflection profiles for different ϕ at $\theta = \frac{5\pi}{12}$, corresponding to mode (ii). As $\Delta\phi$ approaches $\frac{\pi}{2}$, undulations indicate twisting of the sheet. *Inset*: 2D projection of simulated sheet with $\theta = \frac{5\pi}{12}$ and $\Delta\phi = \frac{\pi}{2}$, as an example of large mode (ii) deflection; profiles evaluated along dashed line. (*E*) Curves indicate the deflection in each of the two modes, corresponding to the maximum deflection of the pure modes (i) (orange) or (ii) (purple) at each θ, multiplied by the mode weight a_i or a_{ii} as a function of $\Delta\phi$, where darker lines of either color correspond to lower θ. The contribution of modes i or ii can be tuned by reorienting the field.

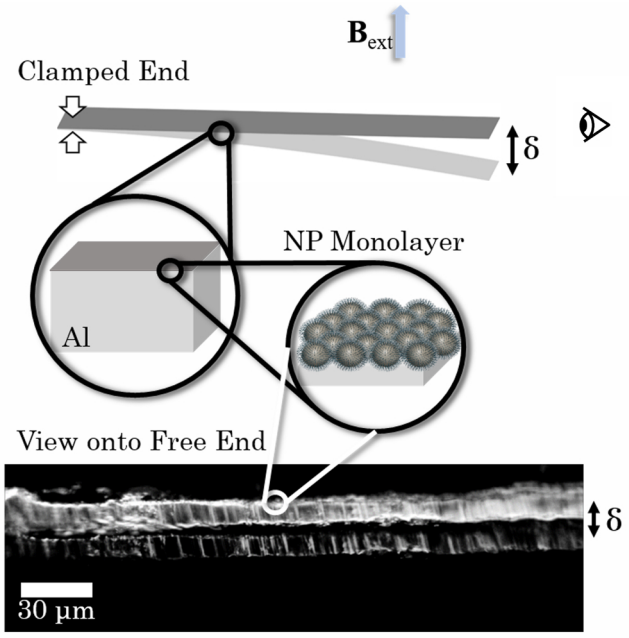

Fig. 6. Actuating NP coated Aluminum. Fe_3O_4 NPs can be used as a surface coating to actuate nonmagnetic structures. We demonstrate this by deflecting an aluminum sheet using a nanoparticle monolayer as depicted in the schematic. The *Bottom* image is a composite micrograph (magnified 50×) of the free end before and after application of the field. The Al sheet is ∼1,000 times thicker than the monolayer and 50 to 100 times stiffer. Despite this, the NPs generate forces strong enough to deflect the Al sheet by $\delta/t_{Al} \sim 1$.

at each θ as a function of $\Delta\phi$ by fitting the superposition of the two pure modes for the other values of $\Delta\phi$. Fig. 5*E* shows the maximum deflection in each of the pure modes weighted by a_i and a_{ii} respectively as $\Delta\phi$ increases from 0, indicating the amount of deflection coming from each mode at each field orientation. The different traces correspond to different values of the polar angle θ. Mode (i) dominates the deflection for most field orientations, but vanishes once the field approaches the fixed diagonal.

NP Sheets Coating Elastic Structures. NP sheets are able to conform to high aspect ratio surface topographies (41) and could therefore find wide use as magnetically responsive coatings to actuate many other types of nanostructures. As a demonstration of the strength of field-induced forces that can be produced by self-assembled Fe_3O_4 NP sheets, we use them to coat much thicker sheets of nonmagnetic material. Fig. 6 shows this with an aluminum sheet of thickness $t_{Al} \sim 15$ μm and Young's modulus $E_{Al} \sim 68$ GPa being deflected in a uniform external magnetic field of strength 0.12 T due to the dipole pressures generated by a NP monolayer of thickness $t_{NP} \sim 12.25$ nm and typical stiffness of 0.5 to 1 GPa deposited on the Al surface. Being $t_{Al}/t_{NP} \sim 1{,}000$ times thicker and $E_{Al}/E_{NP} \sim 50$ to 100 times stiffer than the NP sheet, the aluminum dominates the bending response of the combined structure. Nevertheless, the high areal density of NPs leads to dipole forces sufficient to deflect the aluminum sheet by $\delta/t_{Al} \sim 1$. This response can be further enhanced by sequentially depositing additional NP monolayers.

Conclusions

Our results demonstrate that thin elastic sheets comprising densely packed paramagnetic nanoparticles can exhibit large deflections deep into the nonlinear plate bending regime even in uniform applied magnetic fields. We find that deflections follow a characteristic $\delta \sim B_{ext}^{1.8}$ curve for small fields while saturating for large fields, so that bending deflections measured for sheets with different magnetic and elastic parameters can be collapsed onto a single master curve (Fig. 2). We show how, as a result of strong interparticle dipole interactions, the magnetization response depends on the sheet's orientation with respect to the applied field (Fig. 3) and that the distribution of these magnetizations across the sheet leads to large nonuniform forces (Fig. 4). We also show how rotation of the applied field can generate more complex actuation, such as twisting (Fig. 5).

Constituting the ultrathin limit of self-assembled nanoparticle systems, the monolayer sheets discussed here are the thinnest nanoparticle-based magnetoelastic composites with paramagnetic elements. Magnetic NP sheets allow external control and actuation of nano-scale systems due to their thinness and bending flexibility, and they may be used in a wide range of potential applications for magnetically controlled nano- or micromechanical manipulation. This could enable smaller magnetic soft robotic systems, for which the ability to activate bending and twisting modes by field rotation may prove especially useful in generating motion.

Materials and Methods

Experiments. 12.25 nm Fe_3O_4 nanoparticles are synthesized according to the Sun protocol (42) (see *SI Appendix* for full description). With diameter substantially less than 25 to 30 nm, these particles are well into the superparamagnetic size regime for Fe_3O_4 (43). Following the synthesis, the particles are dispersed in toluene. Quasi-2D nanoparticle sheets are then made through an evaporative self-assembly process adapted from earlier work involving sheets of thiol-coated gold nanoparticles (37). Briefly, a support structure (typically a copper TEM grid with 20 μm square holes) is immersed in a 50 μL droplet of Ultrapure water on a PTFE substrate. A 1 μL droplet of the toluene/NP solution is gently contacted with the water droplet. The toluene coats the water droplet in a thin film, and as it evaporates the nanoparticles in the toluene film are trapped at the air–water interface. Following the rapid evaporation of the toluene and the formation of the NP monolayer at the air–water interface, the water evaporates slowly, gently draping the nanoparticle layer onto the support structure within the water droplet. Once the water completely evaporates, portions of the nanoparticle layer that have torn partially free from the support structure (typically a square with two adjacent free edges) are identified and scanned with a LEXT OLS-5000 confocal surface scanning microscope, with x-y resolution of 125 nm × 125 nm per pixel and nominal z resolution of 10 nm. Since the interparticle separation is 15.75 nm, there are roughly 80 NPs per pixel. Scans are performed with varying external magnetic field strengths and orientations using permanent magnets. Quasi-uniform magnetic fields are generated with arrays of NdFeB magnets in the dipolar cylindrical Halbach configuration, to which larger magnets can be added to generate stronger fields. To avoid contact with the microscope objective, half cylinders are used for generating vertical fields. Small and large half cylinders are used with additional magnets and in combination with each other to generate the different field strengths, which are measured with a linear Hall sensor. Gradients due to permanent magnets are measured with a pair of Hall sensors. The largest such gradients could lead to maximum per-particle forces, for fully saturated particles, that are still ∼100× smaller than the typical dipole–dipole forces described in the main text. See *SI Appendix* for more on the production and measurement of the fields, and the potential impact of external gradients.

Simulations and Modeling. MD simulations are performed using ESPResSo v4.2 (44). The simulated sheets consist of a triangular lattice of hard spheres making up a square of side length 180 particle diameters resulting in a total of 22,680 particles. Simulated sheets correspond to a physical size of 2.2 μm × 2.2 μm. These sheets are initially flat and all particles along the $\hat{\mathbf{x}}$ and $\hat{\mathbf{y}}$ axes are held fixed to mimic the experimental boundary conditions.

As in earlier work, particles interact elastically with their neighbors through a two-body stretching potential $u_s = \frac{\sqrt{3}}{4}Et(r - r_0)^2$, where r_0 is the interparticle separation at rest, and through a four-body bending potential $u_b = \frac{Et^3}{6\sqrt{3}(1-\nu^2)}[1 - \cos(\theta)]$, penalizing angular deviations between the normal vectors of neighboring elements (45). Particles are assumed to behave as point paramagnets. We use a mutual dipole model in which the field due to all the other dipoles in the sheet is also included when determining the dipole magnitudes and directions (28, 34, 46). To determine the particle magnetizations, we solve the set of N coupled nonlinear equations $\mathbf{m}_i = m_{sat}\mathcal{L}(|\mathbf{B}_i|/B_{sat})\hat{\mathbf{B}}_i$ directly. This last step sets the limit on computational speed by far. However, the MDM converges to the same configuration and magnetization regardless of whether the sheet is initially flat or bent, so to generate a relatively quick initial estimate of the final configuration and magnetic state we use an alternate model not previously seen in the literature, which we call the semi-Independent Dipole Model (sIDM). Whereas the MDM assumes $\mathbf{m}_i = m_{sat}\mathcal{L}(|\mathbf{B}_i|/B_{sat})\hat{\mathbf{B}}_i$, the sIDM instead assumes $\mathbf{m}_i = m_{sat}\mathcal{L}(B_{ext}/B_{sat})\hat{\mathbf{B}}_i$, indicating that the direction of the dipoles depends on the total field while the magnitude of the dipoles depends only on the external field. Because the sIDM avoids the nonlinearity connected with the Langevin function, this calculation is much faster. In practice, it can produce nonphysical magnetization states and, thus, magnetic forces (*SI Appendix*, Figs. S2–S5). However, these are only resolved once we switch to the full MDM. Despite this, the final deflections from the sIDM are close to those from the MDM (*SI Appendix*, Fig. S1), and in this way, the sIDM provides a good way to estimate the behavior of a very large system. As shown in Fig. 3 a mathematically flat sheet will not magnetize in a vertical field, so simulations begin with a slight offset to the vertical magnetic field for the first 200 time steps, before finally using a purely vertical field. See *SI Appendix* for further details.

Data, Materials, and Software Availability. All study data are included in the article and/or *SI Appendix* and Materials Data Facility (47).

ACKNOWLEDGMENTS. This work was primarily supported by the University of Chicago Materials Research Science and Engineering Center (MRSEC), which is funded by NSF under award number DMR-2011854. H.M.L.R. acknowledges support from a MRSEC-funded Graduate Research Fellowship. Portions of this manuscript were originally used as part of the dissertation of coauthor H.M.L.R.

Author affiliations: [a]Department of Physics, University of Chicago, Chicago, IL 60637; [b]James Franck Institute, University of Chicago, Chicago, IL 60637; [c]Department of Materials Science and Engineering, Northwestern University, Evanston, IL 60208; [d]Department of Physics and Astronomy, Northwestern University, Evanston, IL 60208; [e]Department of Chemical and Biological Engineering, Northwestern University, Evanston, IL 60208; and [f]Department of Chemistry, Northwestern University, Evanston, IL 60208

1. C. Li *et al.*, Fast and programmable locomotion of hydrogel-metal hybrids under light and magnetic fields. *Sci. Robot.* **5**, eabb9822 (2020).
2. Y. Zhou *et al.*, Giant magnetoelastic effect in soft systems for bioelectronics. *Nat. Mater.* **20**, 1670–1676 (2021).
3. X. Wang *et al.*, Colloidal tubular microrobots for cargo transport and compression. *Proc. Natl. Acad. Sci. U.S.A.* **120**, e2304685120 (2023).
4. G. Hwang *et al.*, Catalytic antimicrobial robots for biofilm eradication. *Sci. Robot.* **4**, eaaw2388 (2019).
5. S. Ponomareva *et al.*, Microstructured magnetoelastic membrane for magnetic bioactuators and soft artificial muscles applications. *Adv. Intell. Syst.* **5**, 2300022 (2023).
6. Z. Qi *et al.*, Reconfigurable flexible electronics driven by origami magnetic membranes. *Adv. Mater. Technol.* **6**, 2001124 (2021).
7. Y. Kim, X. Zhao, Magnetic soft materials and robots. *Chem. Rev.* **122**, 5317–5364 (2022).
8. R. Zhao, Y. Kim, S. A. Chester, P. Sharma, X. Zhao, Mechanics of hard-magnetic soft materials. *J. Mech. Phys. Solids* **124**, 244–263 (2019).
9. R. M. Erb, J. J. Martin, R. Soheilian, C. Pan, J. R. Barber, Actuating soft matter with magnetic torque. *Adv. Funct. Mater.* **26**, 3859–3880 (2016).
10. M. Ha *et al.*, Reconfigurable magnetic origami actuators with on-board sensing for guided assembly. *Adv. Mater.* **33**, 2008751 (2021).
11. C. L. Smart *et al.*, Magnetically programmed diffractive robotics. *Science* **386**, 1031–1037 (2024).
12. T. Yang *et al.*, Reconfigurable microbots folded from simple colloidal chains. *Proc. Natl. Acad. Sci. U.S.A.* **117**, 18186–18193 (2020).
13. L. Lu, J. Sim, R. R. Zhao, Mechanics of hard-magnetic soft materials: A review. *Mech. Mater.* **189**, 104874 (2024).
14. L. Dorfmann, R. W. Ogden, Hard-magnetic soft magnetoelastic materials: Energy considerations. *Int. J. Solids Struct.* **294**, 112789 (2024).
15. D. J. Steigmann, Equilibrium theory for magnetic elastomers and magnetoelastic membranes. *Int. J. Non-Linear Mech.* **39**, 1193–1216 (2004).
16. C. P. Bean, J. D. Livingston, Superparamagnetism. *J. Appl. Phys.* **30**, S120–S129 (1959).
17. G. Maugin, C. Goudjo, The equations of soft-ferromagnetic elastic plates. *Int. J. Solids Struct.* **18**, 889–912 (1982).
18. Y. H. Zhou, X. Zheng, A general expression of magnetic force for soft ferromagnetic plates in complex magnetic fields. *Int. J. Eng. Sci.* **35**, 1405–1417 (1997).
19. C. Li *et al.*, Fast and programmable locomotion of hydrogel-metal hybrids under light and magnetic fields. *Sci. Robot.* **5**, eabb9822 (2020).
20. F. Gerbal *et al.*, A refined theory of magnetoelastic buckling matches experiments with ferromagnetic and superparamagnetic rods. *Proc. Natl. Acad. Sci. U.S.A.* **112**, 7135–7140 (2015).
21. V. P. Shcherbakov, M. Winklhofer, Bending of magnetic filaments under a magnetic field. *Phys. Rev. E* **70**, 061803 (2004).
22. Y. Wang *et al.*, Mechanical properties of self-assembled nanoparticle membranes: Stretching and bending. *Faraday Discuss.* **181**, 325–338 (2015).
23. J. Chang, K. B. Toga, J. D. Paulsen, N. Menon, T. P. Russell, Thickness dependence of the young's modulus of polymer thin films. *Macromolecules* **51**, 6764–6770 (2018).
24. G. Wang *et al.*, Mechanical size effect of freestanding nanoconfined polymer films. *Macromolecules* **55**, 1248–1259 (2022).
25. P. Vázquez-Montejo, M. O. De La Cruz, Flexible paramagnetic membranes in fast precessing fields. *Phys. Rev. E* **98**, 032603 (2018).
26. C. A. Brisbois, M. Tasinkevych, P. Vázquez-Montejo, M. Olvera De La Cruz, Actuation of magnetoelastic membranes in precessing magnetic fields. *Proc. Natl. Acad. Sci. U.S.A.* **116**, 2500–2505 (2019).
27. C. A. Brisbois, M. O. De La Cruz, Locomotion of magnetoelastic membranes in viscous fluids. *Phys. Rev. Res.* **4**, 023166 (2022).
28. E. E. Keaveny, M. R. Maxey, Modeling the magnetic interactions between paramagnetic beads in magnetorheological fluids. *J. Comput. Phys.* **227**, 9554–9571 (2008).
29. J. Faraudo, J. S. Andreu, C. Calero, J. Camacho, Predicting the self-assembly of superparamagnetic colloids under magnetic fields. *Adv. Funct. Mater.* **26**, 3837–3858 (2016).
30. A. Spatafora-Salazar, D. M. Lobmeyer, L. H. P. Cunha, K. Joshi, S. L. Biswal, Hierarchical assemblies of superparamagnetic colloids in time-varying magnetic fields. *Soft Matter* **17**, 1120–1155 (2021).
31. H. E. H. Meijer, L. E. Govaert, Mechanical performance of polymer systems: The relation between structure and properties. *Prog. Polym. Sci.* **30**, 915–938 (2005).
32. L. D. Landau, E. M. Lifshitz, *Theory of elasticity, Course of Theoretical Physics* (Elsevier, 2012), vol. 7.
33. H. Mamiya *et al.*, Estimation of magnetic anisotropy of individual magnetite nanoparticles for magnetic hyperthermia. *ACS Nano* **14**, 8421–8432 (2020).
34. Z. M. Sherman, D. Ghosh, J. W. Swan, Field-directed self-assembly of mutually polarizable nanoparticles. *Langmuir* **34**, 7117–7134 (2018).
35. T. Leps, C. Hartzell, High fidelity, discrete element method simulation of magnetorheological fluids using accurate particle size distributions in liggghts extended with mutual dipole method. *Mater. Res. Express* **8**, 085701 (2021).
36. C. Fernandes, S. A. Faroughi, Particle-level simulation of magnetorheological fluids: A fully-resolved solver. *Int. J. Multiph. Flow* **169**, 104604 (2023).
37. Y. Wang *et al.*, Thermomechanical response of self-assembled nanoparticle membranes. *ACS Nano* **11**, 8026–8033 (2017).
38. A. Cēbers, I. Javaitis, Bending of flexible magnetic rods. *Phys. Rev. E* **70**, 021404 (2004).
39. A. Cēbers, I. Javaitis, Dynamics of a flexible magnetic chain in a rotating magnetic field. *Phys. Rev. E* **69**, 021404 (2004).
40. W. F. Brown, *Magnetoelastic Interactions* (Springer, 1966).
41. N. P. Mitchell *et al.*, Conforming nanoparticle sheets to surfaces with gaussian curvature. *Soft Matter* **14**, 9107–9117 (2018).
42. S. Sun *et al.*, Monodisperse MFe_2O_4 (M = Fe Co, Mn) Nanoparticles. *J. Am. Chem. Soc.* **126**, 273–279 (2004).
43. Y. A. Koksharov, "Magnetism of nanoparticles: Effects of size, shape, and interactions" in *Magnetic Nanoparticles*, S. P. Gubin, Ed. (Wiley-VCH, 2009), pp. 197–254.
44. F. Weik *et al.*, ESPResSo 4.0 - an extensible software package for simulating soft matter systems. *Eur. Phys. J. Spec. Top.* **227**, 1789–1816 (2019).
45. H. S. Seung, D. R. Nelson, Defects in flexible membranes with crystalline order. *Phys. Rev. A* **38**, 1005–1018 (1988).
46. D. Du, F. Toffoletto, S. L. Biswal, Numerical calculation of interaction forces between paramagnetic colloids in two-dimensional systems. *Phys. Rev. E* **89**, 043306 (2014).
47. E. P. Esposito, H. M. Lopez Rios, M. Olvera de la Cruz, H. M. Jaeger, "Dataset for Actuating Superparamagnetic Nanoparticle Monolayers." Materials Data Facility. https://doi.org/10.18126/b5s9-6r94. Deposited 9 March 2025.